We are IntechOpen, the world's leading publisher of Open Access books Built by scientists, for scientists

6,900
Open access books available

186,000
International authors and editors

200M
Downloads

154
Countries delivered to

Our authors are among the

TOP 1%
most cited scientists

12.2%
Contributors from top 500 universities

CLARIVATE ANALYTICS
BOOK CITATION INDEX
INDEXED

WEB OF SCIENCE™

Selection of our books indexed in the Book Citation Index
in Web of Science™ Core Collection (BKCI)

Interested in publishing with us?
Contact book.department@intechopen.com

Numbers displayed above are based on latest data collected.
For more information visit www.intechopen.com

Remotely Monitoring Uranium-Enrichment Plants with Detection of Gaseous Uranium Hexafluoride and HF Using Lidar

Gholamreza Shayeganrad

Abstract

A sudden release of UF_6 inside a building or to the atmosphere could conceivably cause undesirable health effects to workers and the public in general, mainly associated with the exposure to hydrolysis products HF and UO_2F_2. Although the hydrolysis reaction of UF_6 is fast, after escaping of UF_6 into the atmosphere, besides HF and UO_2F_2, UF_6 may also be found in the atmosphere. This chapter proposes a real-time technique to provide information to technical personnel and facility operators on the atmospheric release of UF_6 to ensure that the workers, the public, and the environment are adequately protected. The system comprises a combined differential absorption lidar (DIAL) and Raman lidar to detect gaseous UF_6 and HF, simultaneously. The DIAL provides information on UF_6 concentration using a frequency-quadrupled Nd:YAG laser at 266 nm as the off-wavelength and a Nd:-YAG-pumped Coumarin 450 dye laser using a Littrow grating mounting operating in the frequency doubled at 245 nm as the on-wavelength. Recording Raman scattering of molecular HF at wavelength of 297.3 nm (with Raman frequency shift of 3959 cm^{-1}) is a versatile technique to identify HF as a probe for real-time detection and localization of UF_6 leaks.

Keywords: uranium hexafluoride, hydrogen fluoride, uranium-enrichment plants, fuel cycle facilities, differential absorption lidar (DIAL), Raman lidar

1. Introduction

The raw material for today's nuclear fuel is uranium which first discovered in eighteenth century. Natural uranium consists primarily of two isotopes, 99.3% is U-238 and 0.7% is U-235. The fission process, by which heat energy is released in a nuclear reactor, takes place

mainly in U-235 which can sustain a chain reaction; a reaction in which each fission produces enough neutrons to trigger another, so that the fission process can maintain without any external source of neutrons. In contrast, uranium-238 cannot sustain a chain reaction, but it can be converted to plutonium-239 by high-energy neutrons, which can sustain a chain reaction and release large amounts of energy and is therefore often used to enhance the explosive power of thermonuclear, or hydrogen, bombs [1]. Plutonium-239, virtually nonexistent in nature, was used in the first atomic bomb tested July 16, 1945 and in the one that was dropped on Nagasaki on August 9, 1945. U-234 is a highly radioactive, but it is not useful in any applications.

In 1938, German physicists Otto Hahn and Fritz Strassmann showed that uranium could split into parts to yield lighter elements, neutrons, and energy. For instance, U-238, with half-life of about 4.5 billion years, decays by alpha emission into daughters like thorium-234, which itself decays by beta emission to protactinium-234, which decays by beta emission to uranium-234, and so on. After several more alpha and beta decays, the series ends with the stable isotope lead-206 [1]. Alpha particles have less penetrating than other forms of radiations and weak gamma rays. As long as uranium remains outside the body, it poses little health hazard (mainly from the gamma-rays). If inhaled or ingested, however, its radioactivity poses increased risks of lung cancer and bone cancer. Uranium is also chemically toxic at high concentrations and can cause damage to internal organs, notably the kidneys.

Most nuclear power plants require fuel with U-235 enriched to a level of 3–5%. The uranium fuel cycle begins with the mining and milling uranium ore to produce "yellow cake," a yellow powder of uranium oxide (U_3O_8), which is shipped to conversion facilities for converting to UF_6; the form in which uranium is accepted at current isotope enrichment plants. UF_6 gas is filled into large cylinders where it solidifies. The cylinders are loaded into strong metal containers and shipped to the uranium-enrichment plant. After enrichment, UF_6 is chemically converted to uranium dioxide (UO_2) or metal. Yellow cake has a pungent odor, is insoluble in water, and contains about 80% UO_2, which melts at approximately 2880°C.

A major concern in nuclear fuel cycle facilities, therefore, is the potential of accidental release of UF_6 inside a building or to the atmosphere. UF_6 is rapidly hydrolyzed by ambient moisture to form HF and uranyl fluoride (UO_2F_2). HF is not in itself radioactive; however, it is an extremely corrosive substance that causes severe skin burns, damage to the eyes, and lung injury when inhaled. The effect from acute exposure to HF is a function of the HF concentration and the exposure time. The accumulation of HF in the atmosphere may attack carbon steel and cause corrosion, rupture, or worker exposure via inhalation and skin problem. UO_2F_2 is a water-soluble compound, which in addition to being radioactive can also have toxic chemical effects. If ingested or inhaled, it will enter the bloodstream and will act primarily on the kidneys.

Conversion and enrichment facilities have had a number of accidents involving uranium hexafluoride. One such accident at the Sequoyah Fuels conversion plant in Gore, Oklahoma, on January 4, 1986, killed one worker, hospitalized 37 of the 42 onsite workers, and sent approximately 100 residents to the hospital as well [3]. The most important steps in

the nuclear fuel cycle, namely, uranium refining, conversion, and enrichment, involve the production, handling, transportation, and waste management of UF_6 and related products. Due to the hazardous properties (radioactive, corrosive, and toxic) of UF_6, these operations must be carried out in a safe manner to protect plant workers, the public, and the environment.

It should be pointed out that UF_6 concentration in the environment should be restricted to less than 0.2 mg/m^3 or 13.8 ppb [2]. A common problem associated with the complex flow systems is the detection of gas leaks that cannot be directly observed. At present, there is no common and sensitive remote sensor for real-time monitoring the health and safeguarding uranium enrichment plants. To the author's knowledge, there are some passive and time-consuming methods utilizing the nondestructive measurement of U-235 and U-238 concentrations (or evaluation U-235/U-238 isotope ratio) known as "enrichment meter" based on detection main gamma radiation at 185.7 and 1001.0 keV, respectively [3, 4]. This method can be used on UF_6 released into the atmosphere with either germanium or NaI detector-based systems [5] but is limited in accuracy and requires calibration for each type of sample material and range. Although the 186- and 1001-keV peaks are easy to measure, it is difficult to determine the relative detection efficiency of these two gamma rays because of the large difference in their energies. On the other hand, laser-induced fluorescence can be used for remotely measuring UO_2F_2 concentration. This technique can provide specific chemical information like Raman scattering method; however, the fluorescence of solid-phase uranyl appears to be strongly affected by crystal properties and the extent of hydration [6]. Another method is elastic Mie scattering combined with absorption spectroscopy. The uranyl ion absorption near 10.5 μm overlaps a major lasing transition of the CO_2 laser, which can be used for detection of uranyl fluoride aerosol with minimal interference from major atmospheric gases. However, this wavelength is large relative to the average sizes of UO_2F_2 in the released Uf_6 plume, and thus, the intensity of the scattered light is very weak (Mie scattering).

In the previous works, we proposed an UV-DIAL for measuring UF_6 concentration in the atmosphere [7, 8]. In the UV region, signal to noise ratio (SNR) can be enhanced due to the varying of the Rayleigh and Raman backscattered signal as λ^{-4}, where λ is wavelength. Also, available shot-noise limited photomultiplier tubes (PMTs) with a high sensitivity and high-specific detectivity may increase the improvement of SNR in the UV region. UV-DIAL and Raman lidars are the most promising remote sensing techniques with high sensitivity and accuracy for remotely monitoring gaseous uranium hexafluoride [9]. In contrast, Raman lidar has a unique capability to provide additional information on the structure of the molecular species [10]. In Raman scattering, the frequency shifts are characteristic of the molecule and can be used as a molecular fingerprint. It is a weak process, typically only 1 in 10^6–10^8 photons undergo the Raman inelastic scattering event. This drawback may compensate by using a high power and high repetition rate UV laser (in the order of several tens of Hz), telescope with large area, sensitive PMT detector, and decreasing background noise. It should be emphasized that the elastic lidar near the surface detects combined signals of the Rayleigh and the Mie scattering that may limit the quantitative measurement of properties of molecules in the long-path remote sensing. However, in the DIAL technique, the systematic

error due to the aerosol scattering is negligible, and errors may arise when the wavelengths are significantly separated.

In this chapter, a system consists of UV-DIAL and Raman lidar for real-time actively remote monitoring uranium-enrichment plants has been proposed [9]. Because of the fast reaction of UF_6 with water vapor in the atmosphere (see **Figure 1**), simultaneous measurement of UF_6 and HF may decrease the measurement's uncertainty and improve the sensitivity. A green targeting laser diode can be used to visualize and help the operator to determine where is aiming with invisible UV laser beam during the screening. The system comprises a frequency-quadrupled, compact, pulsed Nd:YAG laser at 10 Hz repetition rate for the off-wavelength at 266 nm and a frequency-doubled Nd:YAG-pumped Coumarin 450 using a Blazed grating mounted in Littrow configuration operating in the frequency doubled for the on-wavelength at 245 nm. The grating is invariably used to allow tuning of the laser across the wide gain bandwidth of the laser. Raman scattering measurements of HF at 297.3 nm with Raman frequency shift 3959 cm^{-1} are helpful to identify HF as a probe for real-time detection and localization of toxic UF_6 leaks.

It should be mentioned that the absorption spectroscopy is also utilized for remotely detection of HF at 1.28 μm [12]. However, it has a drawback of inability to distinguish HF and also limitation due to the strong absorption of water vapor in the region which hampers the measurements, especially at relatively low HF concentrations. Hence, because of the very weakness of Raman scattering of water [10], Raman lidar may be a versatile technique to study HF in the wet environment. Moreover, Raman signal and thereby SNR can be significantly enhanced using UV light especially in the solar blind ultraviolet (200 –310 nm). We believe combined UV-DIAL and Raman lidars is a promising and reliable real-time tool for measuring
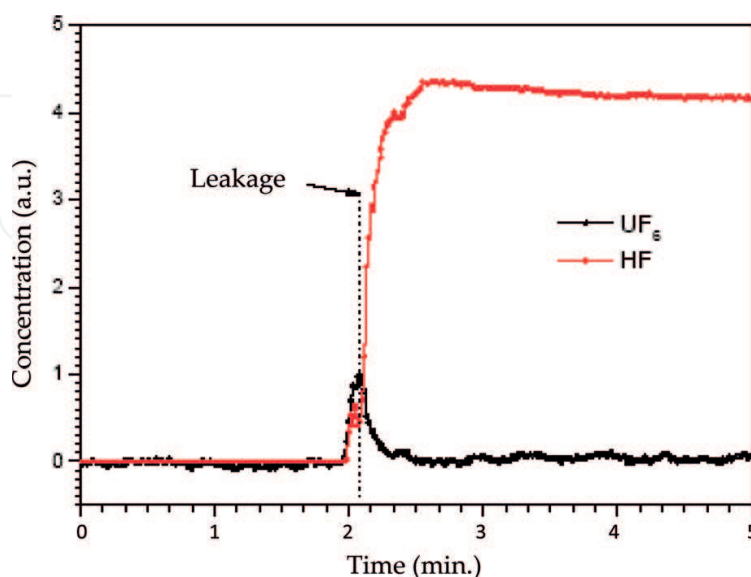

Figure 1. Varying UF_6 and HF concentration in the moisture atmosphere versus time [11].

and tracing UF_6 and HF components in the atmosphere to greatly decrease probable disaster results by releasing gaseous UF_6 in the atmosphere.

2. Physical and chemical properties of UF_6

Uranium hexafluoride can be a solid, liquid, or gas, depending on its temperature and pressure. The phase diagram of UF_6 is schematically shown in **Figure 2**, which presents different physical forms of UF_6 as a function of temperature and pressure [13]. At atmospheric pressure (14.7 psia), UF_6 is a solid below a temperature of 134°F (56.6°C) and a gas at temperatures above 134°F. Liquid UF_6 is formed only at temperatures greater than 147.2°F (64.02°C) and at pressures greater than 1.5 times atmospheric pressure (~22 psia). At atmospheric pressure, solid UF_6 will transform directly to UF_6 gas (sublimation) when the temperature is raised to 134°F, without going through a liquid phase. Detail description on its physical properties can be found in Ref. [14]. All three phases, solid, liquid, and gas, coexist at 64.02°C (147.2°F, the triple point) and P = 1.497 atm. Only the gaseous phase exists above 446°F (230.2°C, the critical temperature), at which critical pressure is 45.5 atm.

Uranium hexafluoride is the substance most suitable for use in the fuel cycle facilities processes because of its exotic physical properties. Since fluorine exists naturally in only one isotopic form (F-19), the physical processes widely used for enrichment of U-235, such as diffusion, centrifugation, and molecular laser isotope separation (MLIS), increase only the concentrations of uranium isotopes. The process of fluorination of uranium dioxide to produce UF_6 can be subdivided into the following chemical reactions:
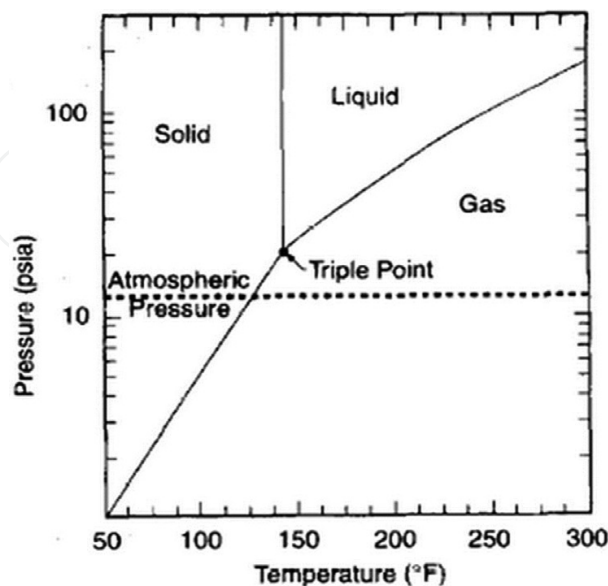

Figure 2. UF_6 phase diagram, showing relationship between pressure, temperature, and physical form [13].

$$U_3O_8 + 2H_2 \rightarrow 3UO_2 + 2H_2O \tag{1}$$

$$UO_2 + 4HF \rightarrow UF_4 + 2H_2O \tag{2}$$

$$UF_4 + F_2 \rightarrow UF_6 \tag{3}$$

The density of UF_6 changes with temperature and for the solid phase can be described by the following equation [15]:

$$\rho_s = 5194 - 5.168T \text{ kg/m}^3 \tag{4}$$

for $0°C \leq T \leq 64°C$. In the liquid state, its density varies in a nonlinear fashion and can be summarized by the following equation [15]:

$$\rho_l = 1670 + 152.03(T_c - T)^{0.5} \text{ kg/m}^3 \tag{5}$$

where $T_c = 230.2°C$, which is accurate close to triple point (T = 64.02°C, p = 1.497 atm), and

$$\rho_l = 2084.3 - 3.1T + 371(T_c - T)^{0.3045} \text{ kg/m}^3 \tag{6}$$

which is more accurate close to the critical point (T = 230°C, p = 45.5 atm). Note that T in Eqs. (4)–(6) is measured in °C.

In the vapor phase, the density of UF_6 can be described according to an equation which is similar in form to the ideal gas law [15]:
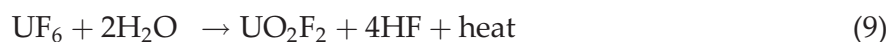
$$\rho_v = \frac{4291p}{T(1 - 1.3769 \times 10^6 p/T^3)} \text{ kg/m}^3 \tag{7}$$

where p is in atm, and T is in K. In the range of 50–140°C, Eq. (8) gives density values [16], which is similar to those obtained using Eq. (7), but it is applicable over a wider temperature range and does not have a singularity limit, i.e.
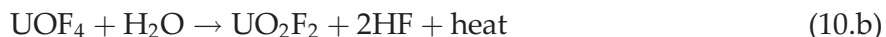
$$\rho_v = \frac{4291p}{T}(1 + 1.2328 \times 10^6 p/T^3) \text{ kg/m}^3 \tag{8}$$

Comparing Eqs. (4) and (5), we can see that during the change from solid to liquid at 64.02°C, a volume expansion of 25.36% takes place (density changes from 4863.25 kg/m^3 (solid) to 3629.95 kg/m^3 (liquid)).

When gaseous UF_6 escapes into the moist atmosphere, it rapidly reacts and hydrolyzes with the ambient water vapor to form hydrogen fluoride (HF) gas and uranyl fluoride (UO_2F_2) particles with diameters of a few microns, both of which are very toxic. This exothermic reaction can be written in the following forms:

$$UF_6 + 2H_2O \rightarrow UO_2F_2 + 4HF + \text{heat} \tag{9}$$

or

$$UF_6 + H_2O \rightarrow UOF_4 + 2HF \qquad (10.a)$$

$$UOF_4 + H_2O \rightarrow UO_2F_2 + 2HF + heat \qquad (10.b)$$

The UF_6 hydrolysis reaction releases approximately 58 kJ/g mole of H_2O, which heats the plume and causes plume rise that afterward slowly sink to the ground. This hydrolysis reaction plays an important role in determining the fate of UF_6 that is released into the atmosphere. If a release occurs inside a building, this fog may impair escape from the release area or may difficult planned emergency actions. A dense fog was observed, for example, at the Hanau conversion plant, in 1987, during a UF_6 release from an autoclave [17]. It has been reported that UO_2F_2 concentrations as low as 1 g/m^3 are visible, and visibility is less than 90 cm [18]. Fog can also occur in unconfined areas if the humidity is high.

The hydrolysis reaction is very fast and is limited by the availability of water. To hydrolyze 1000 kg of UF_6, 100 kg of water is required; at 25°C and 70% relative humidity, this amount of water is contained in 6000 m^3 of air. Following a large-scale release of UF_6 outside, the dispersion is governed by meteorological conditions. The plume could still contain unhydrolyzed UF_6 even after traveling a distance of several 100 meters. In other words, although the hydrolysis reaction of UF_6 is fast, after escaping of UF_6 into the atmosphere, besides HF and UO_2F_2, UF_6 may also be found in the atmosphere. Only escaping a few 100 g of UF_6 into the atmosphere will raise the formation toxic and opaque cloud of uranyl fluoride [19]. UO_2F_2 is a particulate that is very soluble in the lungs, and the uranium acts as a heavy metal poison that can affect the kidneys. HF is an acid vapor that can cause acid burns on the skin or lungs. In the event of an accidental release, its toxicity level can be reached in minutes.

It should be emphasized that enriched UF_6 cannot be directly used in reactors, as it does not withstand high temperatures or pressures. It is therefore converted into UO_2. Fuel pellets are formed by pressing UO_2, which is sintered (baked) at temperatures of over 1400°C to achieve high density and stability. The pellets are cylindrical and are typically 8–15 mm in diameter and 10–15 mm long. They are packed in long metal tubes to form fuel rods, which are grouped in "fuel assemblies" for introduction into a reactor. The spent fuel contains uranium (96%), plutonium (1%), and high-level waste products (3%). The uranium with less than 1% fissile U-235 and the plutonium can be reused. Some countries chemically reprocess usable uranium and plutonium to separate them from unusable waste. Recovered uranium from reprocessing can be returned to the conversion plant, converted to UF_6, and subsequently re-enriched. Recovered plutonium, mixed with uranium, can be used to fabricate mixed oxide fuel (MOX).

3. Materials and methods

A schematic diagram of the combination of DIAL and Raman lidar is shown in **Figure 3**. The description of our DIAL system is provided in details in the earlier papers [8]. The Nd:YAG laser is a Q-switched with pulse repetition rate of 10 Hz and pulsewidth of 10 ns with an output power of several 100 mJ per pulse at the fundamental wavelength, 1064 nm. In the laser unit, the 1064-nm laser beam is sent through the frequency doubling and quadrupling harmonic
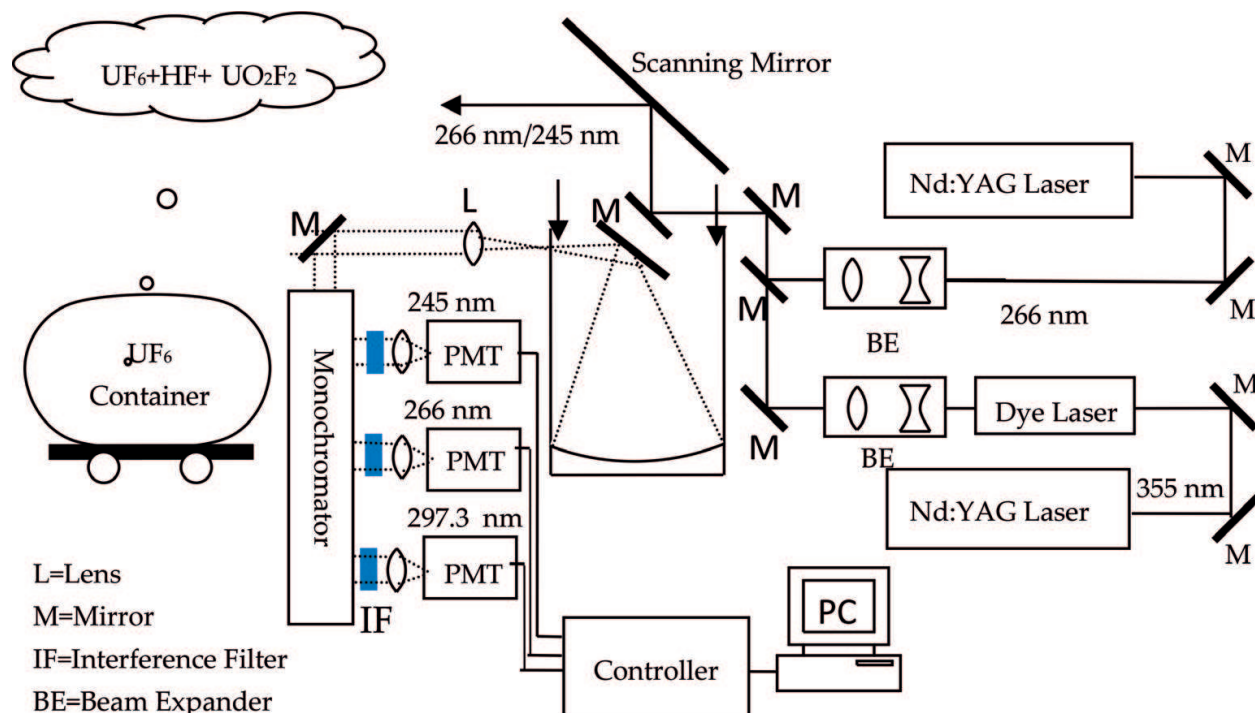
Figure 3. Schematic diagram of the combined differential absorption/Raman lidars for simultaneously remote detection of UF_6 and HF.

crystal modules to deliver a laser beam at 266 nm (4th harmonic) for the off-wavelength. A practical reason for choosing fourth harmonic of Nd:YAG laser as off-wavelength is its reliability, compactness, long lifetime, and low running costs. However, its main drawback is the strong absorption by ozone at 266 nm [20].

A frequency-tripled Nd:YAG-pumped Coumarin 450 dye laser using a Littrow grating mounting operates in the frequency doubled mode for the on-wavelength, 245 nm. The grating is invariably used to allow tuning the laser across the wide gain bandwidth of the laser, the biggest advantage of dye lasers. Use of a diffraction grating alone as a wavelength selector (with suitable beam expanding optics allowing utilization of a large area of the grating surface) renders a spectral width of 0.01 nm. To reduce linewidth, an intracavity etalon is often included in the optical path. Use of an etalon along with a diffraction grating can render spectral widths as low as 0.0005 nm [21]. Coumarin 450 dye lasers with the spectral emission 427–488 nm is considered because of tunability, compactness, output stability, design simplicity, and good beam quality. Coumarin 450 has an absorption peak at 366 nm and an emission peak at 440 nm.

The laser output radiations are expanded by a beam expander (BE). The expanded beams are folded 90° by UV-enhanced aluminum-coated mirrors which have a good reflectivity in the region of 250–300 nm (R > 86%) and subsequently steered them toward the UF_6 and hydrolyzed products plume released into the atmosphere. After interaction with particles and molecules of the atmosphere and plume, the elastic and inelastic backscattered radiations at 266, 245, and 297.3 nm are collected by a Newtonian-type telescope. It has an aspheric primary mirror with the focal length F. A secondary flat mirror reflects the converging light through a

diaphragm with a diameter D. An MgF_2 plano-convex lens (L) after the diaphragm is used to provide a collimated beam. The collimated beam after passing through a monochromator is focused on the entrance pupil of the detector through a Lyot tunable birefringent or Fabry-Pérot interference filters (IF). The diaphragm is in the focal plane of the telescope and sets the field of view (FOV) of the receiver, FOV ≈ D/F. To obtain a required FOV, we select the diameter of the diaphragm for a given focal length of the telescope. The FOV of the receiver is usually set small (about 100 micro-radians full angle FOV) to reject the background noise and achieve acceptable SNR.

As mentioned above, along with the power of the laser, the size of the primary optics is an important factor in determining the effectiveness of the system. Since the returned signal from the far distance is relatively weak, to improve the SNR and increase the detection range, a reasonable FOV is essential to suppress the sky background light, especially during the daytime measurements under sunlit conditions. The smaller aperture optics is used to work in close ranges, for example, a few 100 m, where the returned signal is a larger fraction of the transmitted power. To address the minimum distance at which returning signals are completely in the instrument's FOV, the FOV of the instruments needs to be wide enough. The wide field angle of the receiver reduces the overlap range to several 100 meters. However, the increase in FOV increases the collection of unwanted solar background, resulting in unacceptably poor SNR during daytime measurements. One way to reduce the background solar radiation in the wide FOV lidars is working in the solar blind region. Moreover, by adding an AR coating, the overall transmission of the lenses can be increased. The UV folding mirrors also can reduce the nonresonant background noise.

Monochromator is used to separate the signals, and narrowband filters (IF) are used to extract the Raman and elastic signals at 266, 245, and 297.3 nm. Narrow bandpass filters designed for these center wavelengths allow isolation of the Raman line and increase the SNR by rejecting the out-of-band radiations. Some of the channels may use neutral density filters for reducing the signal intensity to a level that does not saturate the PMT. The high-resolution reflection grating of the monochromator diffracts the background noise as well and makes it possible to separate and block the majority of background noises with combination of a small diaphragm. Most detectors have a window or a lens between the active area of the detector and the energy source. The solid angle cone from which energy can reach the detector is determined by the distance of the detector surface from the front surface of the window or by curvature of the lens. Antireflection coatings are applied to the detector materials or, where applicable, windows and lenses to reduce the reflection losses. The acquisition system is based on a three-channel transient digitizer working in the photon counting mode for increased sensitivity at low signal levels.

4. Results and discussion

The total photon counts received by the elastic-DIAL at the distance R from both the aerosol and molecular backscattering species, $N_{sig}(R)$, is given by the general lidar equation:

$$N_{sig}(\lambda_L, R) = \frac{E_L(\lambda_L)}{h\nu} \eta_{tot} \beta(\lambda_L, R) \Delta R \frac{A}{R^2} \exp[-2\tau(\lambda_L, R)] \tag{11}$$

where E_L is the transmitting energy, h and ν are Planck's constant and the laser frequency, $\eta_{tot} = \eta_t \eta_r \eta_{FOV} \eta_{IF} \eta_{PMT}$ is the total efficiency of the lidar, η_t is the transmitting efficiency owing to the beam expander and mirrors, η_r is the receiving efficiency owing to the mirrors, lenses, and telescope, η_{FOV} and η_{IF} are the efficiency of the FOV and interference filters, η_{PMT} is the quantum efficiency of the PMT, ΔR is the range resolution of the photon counter, $\beta(R)$ is the total backscatter coefficient of molecules and aerosols, A is the area of the telescope, and the optical depth or optical thickness $\tau(\lambda, R) = \int_0^R \alpha(\lambda, r)dr$ is the integral of the extinction coefficient $\alpha(\lambda, r)$ along the path which is a function of the laser wavelength and distance.

Usually backscatter coefficient β for elastically backscattered light consists of contribution of both air molecules and aerosols, i.e., $\beta(R) = \beta_{ms}(R) + \beta_{as}(R)$. For molecular species, backscatter and extinction coefficient differs by a constant factor $\beta_{ms} = (3/8\pi)\alpha_{ms}$ and can easily be substituted. While for the aerosol species, this procedure is not possible and must define "lidar-ratio" [22, 23]:

$$S(R) = \frac{\alpha_{as}}{\beta_{as}} \tag{12}$$

The result of the inversion is the backscatter ratio which is defined as:

$$B(R) = \frac{\beta_{as} + \beta_{ms}}{\beta_{ms}} = \frac{8\pi\alpha_{as}}{3\alpha_{ms}}\frac{1}{S} + 1 \tag{13}$$

For a lidar system with a narrow FOV and a separation between transmitter and receiver optical axes, the incomplete overlap between the laser beam and the receiver FOV significantly affects lidar observation in the short range. When separation of the laser and telescope axes is negligible or small enough in which the area of the laser illumination lies totally within the receiver-optical FOV or vice versa, the overlap distance and efficiency may be adjusted by controlling the FOV of the telescope or the divergence of the laser beam (DIV). As the transmitting laser has nearly a TEM_{00} mode Gaussian shape, for a given beam divergence, the FOV receiving efficiency, η_{FOV}, increases with FOV and saturates for FOV ≥ 1.5DIV as described in Eq. (14), which can be derived from the integral of the radial intensity distribution of TEM_{00} mode:

$$\eta_{FOV} = 1 - \exp\left(-2\frac{FOV^2}{DIV^2}\right) \tag{14}$$

It indicates that the FOV of the telescope optics must be larger than the laser beam divergence so that the lidar can see the entire illuminated volume.

The volume density N_{spcies} (in ppb) of the measurement target species in the range between R and R + ΔR can be derived from Eq. (15), which is known as the DIAL equation:

$$N_{species} = \frac{10^9}{2N_{atm}\Delta\sigma}\frac{\partial}{\partial R}\ln\left[\frac{N_{sig}(\lambda_{off},R)}{N_{sigs}(\lambda_{on},R)}\right] - \frac{10^9}{2N_{atm}\Delta\sigma}\frac{\partial}{\partial R}\ln\left[\frac{\beta(\lambda_{off},R)}{\beta(\lambda_{on},R)}\right] - \frac{\Delta\alpha_{atm}}{N_{atm}\Delta\sigma}\times 10^9 \quad (15)$$

Here $\Delta\sigma = \sigma_{abs}(\lambda_{on}) - \sigma_{abs}(\lambda_{off})$ is the differential absorption cross-section of the species of interest, and $N_{atm} = 2.55 \times 10^{19}$ cm^{-3} is the total number density of molecules in the atmosphere at sea level. At 266 nm, the absorption cross section of UF$_6$ appears to be constant, $\sigma = (1.15 \pm 0.01) \times 10^{-18}$ cm^2 from 0 to 100°C. The absorption cross section at 245 nm over the same temperature range may be represented with the empirical polynomial $\sigma = [1.37 \pm 0.05 + (9.7 \pm 1.5) \times 10^{-3}.T - (4.2 \pm 1.1)10^{-5}.T^2] \times 10^{-18}$ cm^2, where T is in degrees Celsius [24]. One can obtain the differential absorption cross section of $\Delta\sigma = 4.2 \times 10^{-19}$ cm^2 at room temperature T = 23°C for λ_{on} = 245 nm and λ_{off} = 266 nm. Since aerosol concentration is typically high enough near the ground surface, it is reasonable to approximate $\beta = \beta_{as}$. For the horizontal homogenous atmospheric path, β_{as} is a slowly decreasing function of wavelength; therefore, the second term on the right hand side of the Eq. (15) can be negligible. However, for wavelengths below 300 nm, the wavelength dependent aerosol backscatter coefficient, β_{as}, can significantly deviate from λ^{-1} law, depending on the aerosol type. Therefore, a long distance between λ_{on} and λ_{off} can introduce noticeable systematic error in regions of the atmosphere, where the aerosol size gradient is large.

In Eq. (15), $\Delta\alpha_{atm} = \alpha_{atm}(\lambda_{off}) - \alpha_{atm}(\lambda_{on})$ is the differential extinction coefficient of the atmosphere, described as:

$$\begin{aligned}\Delta\alpha_{atm} = \Delta\alpha_{ma} + \Delta\alpha_{ms} + \Delta\alpha_{as} &= [\alpha_{ma}(\lambda_{off},R) - \alpha_{ma}(\lambda_{on},R)] \\ &+ [\alpha_{ms}(\lambda_{off},R) - \alpha_{ms}(\lambda_{on},R)] \\ &+ [\alpha_{as}(\lambda_{off},R) - \alpha_{as}(\lambda_{on},R)]\end{aligned} \quad (16)$$

where $\Delta\alpha_{ma}$, $\Delta\alpha_{ms}$, and $\Delta\alpha_{as}$ are the differential molecular absorption, molecular scattering, and aerosol scattering coefficients, respectively. The measurement accuracy of DIAL depends very strongly on accuracy of species absorption cross-section and evolution of atmospheric extinction. The main errors of the measurement gas concentration lie with the high aerosol and air molecule concentrations in the troposphere, and errors are caused by the large wavelength separation between the "on" and "off" signals and different absorption by gases other than the species of interest and scattering caused by aerosols and molecules. Simplifying conditions can be hold when the "on" and "off" wavelengths are much more close together, and differential extinction coefficient of the atmosphere is negligible. In addition, differential backscatter error is negligible under the condition of spatially homogeneous backscatter. If the simplifications cannot be made, each of the error terms must be considered [20]. The total error caused from the atmosphere for detection UF$_6$ can be obtained as:

$$Error_{atm}(ppb) = 1.3 \times 10^8(\Delta\alpha_{ms} + \Delta\alpha_{ma} + \Delta\alpha_{as}) \quad (17)$$

Among the expected noise from constituents in the atmosphere, O$_3$ is considered as the dominant constituent in the UV region. **Figure 4** shows ozone absorption extinction as a function of
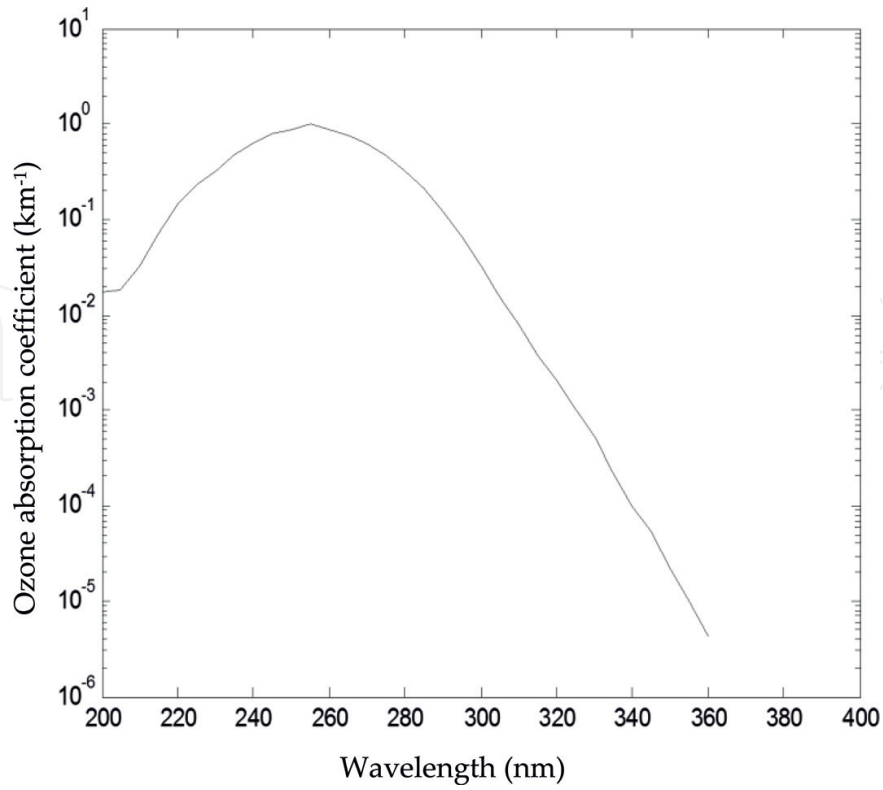
Figure 4. The ozone absorption extinction as a function of wavelength [20].

wavelength in the UV region. The ozone concentration near the surface is considered to be about 0.8×10^{12} cm^{-3}, corresponding to 30 µg/cm^{-3} or 30 parts in 10^9 volumes (ppbv). From ~200 to ~310 nm, the ozone absorption coefficient is large with a maximum absorption extinction ~1 km^{-1} at 255 nm, and it reduces rapidly to ~10^{-6} km^{-1} by increasing wavelength near 360 nm [20, 25].

Before designing a DIAL system, the differential absorption of the target species must be known to derive the necessary parameters such as laser energy, linewidth, and detector area. Also, the sensitivity and lower detection limit of the DIAL measurement are directly dependent on the accuracy of the differential absorption cross-section. From Eq. (15), it follows that if differential extinction and backscatter coefficients of the atmosphere as a function of wavelength are known, a measurement of backscatter power is adequate to precisely determine concentration.

In photodetectors, such as PMT or APD, that have an internal gain, both signal and noise are amplified. Usually, in photon counting regime, the random errors caused by shot noise is the dominant factor to fluctuate the detected signal and background. The SNR at each wavelength can be computed for each laser shot from:

$$SNR_i = \frac{N_{sig}}{\sqrt{N_{sig} + N_{bg} + N_n}} \qquad (18)$$

where N_{bg}, N_n, and N_{sig} are the detected background, dark counts accumulated over the laser pulsewidth, and the detected signal photons, respectively. From Eq. (18), the SNR is maximum when $N_n = N_{bg} = 0$; i.e., $SNR_{max} = \sqrt{N_{sig}}$. The SNR decreases rapidly once the received light intensity drops below the noise intensity.

The total detector noise counts within the laser pulsewidth, N, which is caused by the detected sunlight and the detector dark noise, is given by:

$$N = N_{bg} + \dot{N}_d \tau_{PMT} \tag{19}$$

where dN_d/dt is the detector dark noise count rate (Hz), τ_{PMT} is the PMT response time constant or receiver pulse integration time, usually slightly larger than the laser pulsewidth, and N_{bg} is the photon counts of the background light received by the lidar is expressed by:

$$N_{bg} = \frac{1}{h\nu}\eta_r\eta_{IF}\eta_{PMT}B_{bg}\Omega A\Delta\lambda_{BIF}\tau_{PMT} \tag{20}$$

where B_{bg} is the sky background radiation that is negligible in the solar blind region, $\Delta\lambda_{BIF}$ is the bandwidth of the narrow-band interference filter, and $\Omega = \pi FOV^2/4$ is the viewing solid angle. For a low dark count detector in the solar blind region, total detector noise count can be approximated as $N \approx 0$. After accumulating photon counts for an integration time T_{int}, the averaged SNR at each wavelength is given by:

$$SNR(\lambda_i) = \sqrt{f(\lambda_i)_{las}T_{int}}SNR_i \tag{21.a}$$

where $f(\lambda)_{las}$ is the laser repetition rate at wavelength λ, and $f(\lambda)_{las}T_{int}$ is the total number of pulse measurements averaged. For a low dark count detector in the solar blind region, we can simplify Eq. (21.a) as below:

$$SNR(\lambda_i) = \sqrt{f(\lambda_i)_{las}T_{int}}\sqrt{N_{sig}} \tag{21.b}$$

The feasibility of the system is simulated by taking into account the contribution of molecules and aerosols in the backscatter lidar photon rate. The aerosol backscatter has been included in the simulation considering the lidar ratio of 50 Sr corresponding to extinction and back-scattered coefficients of 5×10^{-4} m^{-1} and 1×10^{-5} m^{-1}Sr^{-1}, respectively. The simulation results are organized using the parameter introduced in **Table 1**. In **Figure 5**, the minimum detectable concentration of UF$_6$ as a function of range for a typical detector having a low SNR of 1.5 is depicted. It can be seen that the minimum detectable concentration of UF$_6$ is limited to 1.21 ppm for range of 1000 m. Note that each system parameter should be carefully considered in a trade-off analyses, including the distances (or ranges) from which the measurements are to be taken, to determine the best overall solution for a given lidar application. In other words, if the determined set of lidar parameters yields a SNR that is below specification, it may be adjusted simply by reducing the DIV, and thus, the SNR will increase, or by increasing the integration time (number of shots) as shown in **Figure 6**. It may also possibly increase the

Transmitting subsystems	
Energy per pulse	300 mJ
Repetition rate	10 Hz
Pulsewidth (FWHM)	10 ns
Pulse laser linewidth (FWHM)	0.1 nm
Optical transmission efficiency	0.7
Far-Field Full angle divergence (beam expanded)	100 µRad
Receiving subsystems	
Telescope aperture (diameter)	35 cm
FOV	200 µRad
Interference filter bandwidth	0.1 nm
Receiving efficiency	0.5
PMT quantum efficiency	0.1
Range resolution of photon counter	30 m

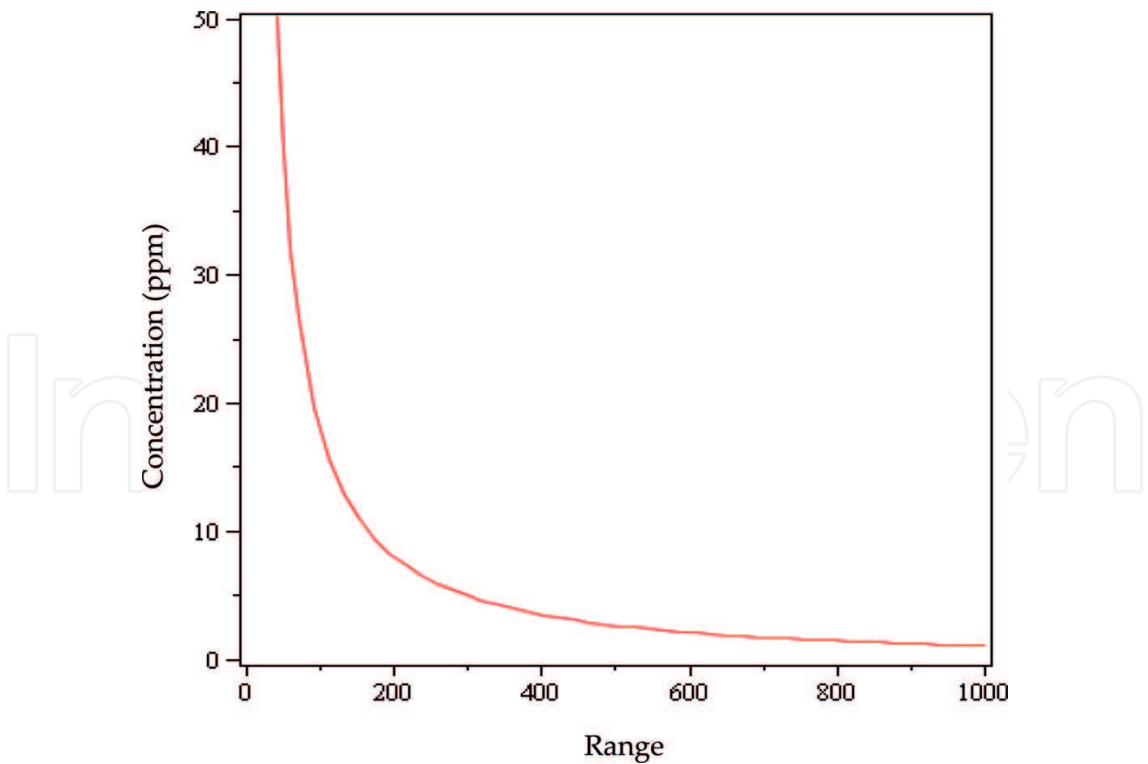**Table 1.** Major parameters of the lidar system considered in simulation.

Figure 5. The minimum detectable UF_6 concentration by DIAL (λ_{on} = 245 nm and λ_{off} = 266 nm) versus range for one pulse for a very low dark count detector. The SNR is considered to be 1.5. Other parameters of the lidar system are shown in **Table 1**.
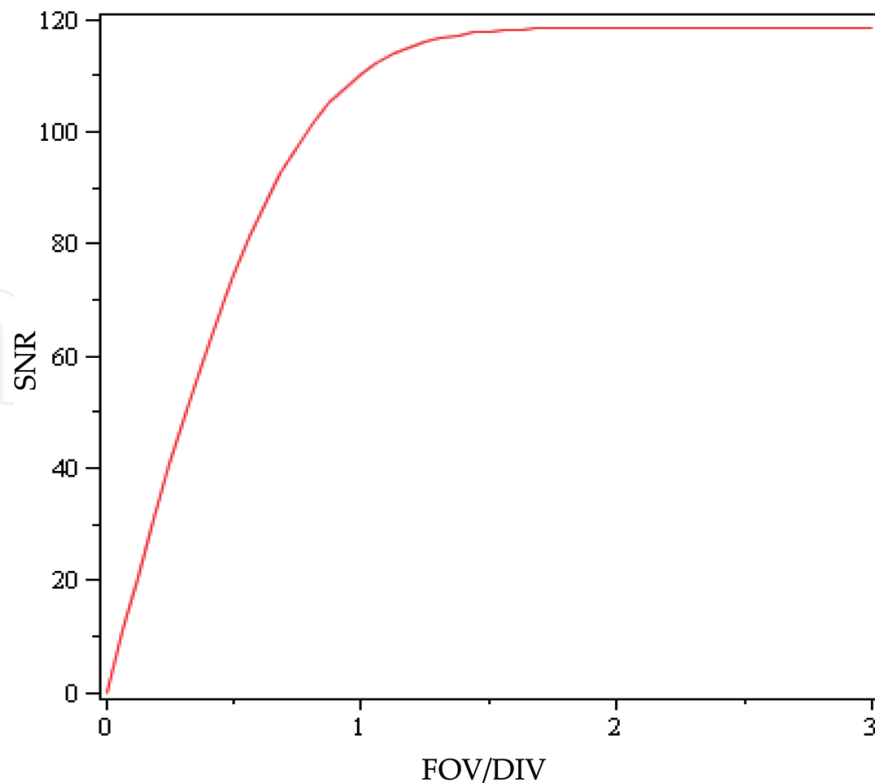
Figure 6. Calculated SNR as a function of FOV/DIV for a UF_6 cloud with 1.1 ppm concentration at 1 km. The integration time is 300 second (3000 shots). Other parameters of the lidar system are shown in **Table 1**.

receiver diameter; however, it increases both the received signal and noise in the same proportion. An increase in the laser beam diameter will increase the received signal, as well as SNR.

Despite the advantage of large Mie- and Rayleigh-scattering and therefore high SNR of the conventional elastic lidar systems, they cannot provide species selectivity. In contrast, inelastic Raman scattering where the frequency of the scattered radiation is shifted by an amount that is a unique of the molecule can be used like fingerprint to distinguish molecular species. In other words, the Raman spectrum contains characteristic signatures of each target molecules with high spectral resolution which makes the Raman spectroscopy a very powerful technique for characterization and identification of unknown species. The intensity of the Raman signal is directly proportional to the density of the scattering molecules independent of other molecular or particulate species:

$$N_{sig}(\lambda_{Ra}, R) = \frac{E_L(\lambda_L)}{h\nu} \eta_{tot} \beta_{Ra}(\lambda_L, R) \Delta R \frac{A}{R^2} \exp[-\tau(\lambda_L, R) - \tau(\lambda_{Ra}, R)] \tag{22}$$

where

$$\beta_{Ra}(\lambda_L, R) = N_{Ra}(R) \frac{d\sigma_{Ra}(\pi, \lambda_L)}{d\Omega} \tag{23}$$

is the Raman backscatter coefficient, λ_L and λ_{Ra} are the wavelength of laser and Raman, respectively. The wavelength shift and also narrow spectral width of the Raman scattered

signal respectively at 266 and 297.3 nm allows distinguishing HF from the other species which elastically scatter 266 nm radiation [10]. Simultaneous measurement of the elastic-backscatter signals at 266 nm and 245 nm and the HF inelastic-backscatter signal at 297.3 nm permit the determination of the concentration of UF_6 and HF, independently, and therefore detection and localization of UF_6 leaks. Notice that both Rayleigh and Raman scattering are two-photon processes involving scattered incident light from a virtual state. The main problem of the Raman scattering is its weak interaction compared to Rayleigh scattering, with a cross-section that is typically 3–4 orders of magnitude smaller. Therefore, the strong Rayleigh scattered radiation must be eliminated when analyzing the weak Raman scattered radiation. The Raman lidar typically consists of an untunable laser excitation source, collection optics like a telescope to collect the rotational-vibrational backscattered radiation from the molecular HF, a spectral analyzer such as monochromator, and a high-sensitive detector such as PMT. The collection optics must be carefully designed to collect as much as the Raman scattered radiation from HF and transfer it into the monochromator. Using a high-sensitive PMT and a high-throughput monochromator with Rayleigh rejection filters may dramatically improve the performance of the Raman lidar. The low intensity of the Raman backscattered signal can be improved by using a high-power laser, high-efficient receiver, low-noise detector, and operation in the solar blind region. It is well known that tropospheric and stratospheric ozone absorb practically all of the incoming solar radiation in this region of the spectrum, providing a black background for detection of the weak Raman signals in the region of 200–310 nm. Natural ozone mainly occurs in the stratosphere between heights of 15 and 50 km. The solar blind region provides conditions that make it possible to operate lidar with a wide FOV telescope and sensitive quantum noise–limited photon counting detectors. The magnitude of the Raman shift is specific of the excited molecule, and the detected light is proportional to the concentration of molecule and Raman cross-section as well. At wavelengths greater than 310 nm, the background noise radiation is significant. Below 200 nm, absorption by oxygen is so strong that propagation is severely limited, and it is not feasible to operate within the atmosphere.

So far, a single grating monochromator and a double grating monochromator in combination with an interference filter have been employed to separate wavelengths effectively in practice [26]. Moreover, for further suppressing the elastic Mie- and Rayleigh-scattering signals, two sets of interference filters can be employed. To improve the optical efficiency of spectroscopic filters, the filters are designed with a peak transmittance at non-normal incidence angle. The function relationship between the central wavelength at normal incidence, λ_n, and wavelength at non-normal incidence angle of θ is given by:

$$\lambda(\theta) = \lambda_n \sqrt{1 - (\sin\theta/n)^2} \tag{24}$$

where n is the effective refractive index of the filter. λ/λ_n decreases slowly with angle from 1 to 0.75, as angle is increased from normal to 90° for the case of n = 1.5. In many applications, angle shifts can be safely ignored. Using a high-index material such as zinc sulfide (n = 2.355 at 632.8 nm), the feature of the spectrum shift to the shorter wavelength versus angle decreases. Sometime, two narrow-band interference filters combined with a high resolution grating are

used to construct a powerful spectroscopic system for achieving the required high rejection rate of 10^7.

The grating diffracts the spectra of the backscattered signal spatially according to the Fraunhofer diffraction. If the incident light beam is not perpendicular to the grooves, the grating equation is given by the modified equation as [27]:

$$Gm\lambda = \cos\gamma(\sin\alpha + \sin\beta) \tag{25}$$

Here, m is diffraction order, α is the angle of incidence, λ is the diffracted light at angle of β, G = 1/d is the groove frequency or groove density, and γ is the angle between the incident light path and the plane perpendicular to the grooves at the grating center. If the incident light lies in this plane, $\gamma = 0$, and Eq. (25) reduces to the famous grating equation. In geometries for which $\gamma \neq 0$, the diffracted spectra lie on a cone rather than in a plane, so such cases are termed conical diffraction. In the most fundamental senses, both spectral bandpass and resolution are used as a measure of an instrument's ability to separate adjacent spectral lines called resolving power. The spectral bandpass is the wavelength interval passed through the exit slit or falls onto the detector. Resolution is related to the bandpass but determines whether the separation of two adjacent peaks can be distinguished. The spectral resolution $\Delta\lambda$ is measured by convolution of the image of the entrance aperture with the exit aperture. It determines resolving power RP = $\lambda/\Delta\lambda$. However, the practical resolving power is limited by the spectral width of the spectral lines emitted by the source.

Spectral bandpass resolved by a monochromator is the difference in wavelength between the points of the half-maximum intensity on either side of the intensity maximum. For an optical system, bandpass is given by:

$$BP = W.R_d \tag{26}$$

where R_d is reciprocal of linear dispersion, and W is the width of the entrance or exit slit (larger one). An instrument with smaller bandpass can resolve wavelengths that are closer together than an instrument with a larger bandpass. Bandpass can be reduced by decreasing the width of the exit slit but usually at the cost of decreasing light intensity. The reciprocal linear dispersion represents the number of wavelength intervals (e.g., nm) contained in each interval of distance (e.g., mm) along the focal plane:

$$R_d = \frac{\partial\lambda}{\partial x} = \frac{d\cos(\beta)}{f.m} \tag{27}$$

where d is the ruled width of grating and f is the focal length of the grating (in the case of curved grating). At small angles of diffraction, Eq. (27) is simplified as:

$$R_d = \frac{d}{f.m} \tag{28}$$

By substituting Eq. (28) into Eq. (26), one can obtain:

$$BP = \frac{W.d}{f.m} \tag{29}$$

For instance, considering G = 1200 gr/mm, W = 0.05 mm, f = 500 mm, and m = 1, the obtained bandpass is 0.083 nm. For selecting grating, one should consider that the grating equation reveals only the spectral orders for which $|m\lambda/d| < 2$ exist. This restriction prevents light of wavelength λ from being diffracted in more than a finite number of order m. Once angle of incidence has been determined, the choice must be made whether a small width grating should be used in a low order, or a large width grating such as an echelle grating should be used in a high order; though, the small width grating will provide a larger free spectral range, $\Delta\lambda_{FSR} = \lambda/m$.

The minimum attainable spectral resolution is given by:

$$\Delta\lambda = \lambda^2/2D \tag{30}$$

regardless of the order m or number of grooves N under illumination. Here D = Nd is the rules width of the grating. This minimum condition corresponds to the grazing Littrow configuration. Noticeably when the grating is incorporated in a spectrometer or monochromator, however, aberrations and imperfections in other elements (e.g., lenses and mirrors) rather than grating and factors related to the size of the slits and detector elements may result in even wider spectral resolution. This means that the minimum wavelength difference $\Delta\lambda$ that can be resolved will be larger that for the grating only defined by Eq. (30), and, in general, the resolving power for the optical system degrades.

5. Conclusion

A sudden release of UF_6 into the atmosphere can conceivably cause undesirable health effects to the workers and the public in general associated with high level of toxicity of the hydrolysis products HF and UO_2F_2. Although the hydrolyze reaction of UF_6 is fast, however, after escaping of UF_6 into the atmosphere, besides HF and UO_2F_2, UF_6 may also be found in the atmosphere. Therefore, the combination of DIAL and Raman lidar for simultaneously detection of UF_6 and HF can be a reliable technique for remotely detection and monitoring UF_6 leaks and further improving the safety and economically operation of a uranium-enrichment plant. The DIAL provides information on UF_6 concentration using the off- and on-wavelength at 266 and 245 nm, respectively, while Raman scattering of HF at 297.3 nm can identify and quantify HF as a probe for real-time detection and localization of toxic UF_6 leaks. This system might be mounted on a helicopter for quickly and remotely surveying the leaks from the large facilities. Since the system is working in the solar blind ultraviolet (200–310 nm), the Raman signal may simply be enhanced by increasing FOV or increasing the integration time (or number of shots).

Author details

Gholamreza Shayeganrad

Address all correspondence to: gholamreza.shayeganrad@unibas.ch; shayeganrad@yahoo.com

Department of Biomedical Engineering, University of Basel, Gewerbestr, Allschwil, Switzerland

References

[1] Knoll GE. Radiation Detection and Measurement. 3rd ed. New York: John Wiley & Sons, Inc; 2000

[2] Safety requrements, Safety of nuclear fuel cycle facilities. IAEA, No. NS-R-5 (Rev.1) 2007

[3] Railly D, Ensslin N, Smith H, eds, Passive Nondestructive Assay on Nuclear Materials. 1991

[4] Reilly TD, Walton RB, Parker JL. A-1 Progress Report LA-4605-MS. 1970. p. 19

[5] Shayeganrad G, Parvin P. DIAL–phoswich hybrid system for remote sensing of radioactive plumes in order to evaluate external dose rate. Progress in Nuclear Energy. 2008;**51**: 420-433

[6] Rabinwitch E, Linn Belford R, Dunworth JV. Spectroscopy and Photochemistry of Uranyl Compounds. Oxford: Program Press; 1964

[7] Shayeganrad G, Mashhadi L. Remote leak detection of UF6 by UV-DIAL. 2009: Iranan Patent, No. 59319

[8] Shayeganrad G, Mashhadi L. High speed remote monitoring of hazardous uranium hexafluoride by lidar. In: Proceedings of the 25th international laser radar conference. 2010: St.-Petersburg. pp. 814-817

[9] Shayeganrad G. On the remote monitoring of gaseous uranium hexafluoride in the lower atmosphere using lidar. Optics and Lasers in Engineering. 2013;**51**:1192-1198

[10] Chalmers JM, Griffiths PK. eds, Handbook of Vibrational Spectroscopy. Chichester: John Wiley & Sons Ltd; 2002

[11] Grigoriev GY et al. Remote detection of HF molecules in open atmosphere with the use of tunable diode lasers. Applied Physics B. 2010;**101**:683-688

[12] Gibson G et al. Remote detection of HF molecules in open atmosphere with the use of tunable diode lasers. Applied Physics B: Lasers and Optics. 2010;**101**:683-688

[13] Hanna SR, Chang JC. Modeling accidental releases to the atmosphere of a dense reactive chemical. Atmospheric Environment. 1997;**31**:901-908

[14] Sazhin SS, Jeapes AP. Fluorination of uranium dioxide particles: A review of physical and chemical properties of the compounds involved. Journal of Nuclear Materials. 1999;**275**: 231-245

[15] Lewis RW, Zheng Y, Gethin DT. An adaptive finite element model for the behaviour of uranium hexafluoride filled container in a fire. Nuclear Engineering and Design. 1993; **140**:229-250

[16] Masi JF. The heats of vaporization of uranium hexafluoride. The Journal of Chemical Physics. 1949;**17**:755

[17] Bayer H. UF_6 Release in a German Fuel Fabrication Plant-Sequence and Consequences. In: Conference Proceedings, Uranium Hexafluoride- Safe Handling, Processing and Transporting, Oak Ridge, Tennessee, USA. 1988

[18] Bouzigues H, et al. The safety problems associated with the handling and storage of UF_6. In: Proceedings of the Specialists Meeting. 1978: Boekelo, The Netherlands. p. 344

[19] Zherin II, Penin ST, Chistyakova LK, Kokhanov VI. Experimental study of the aerosol formation by hydrolysis of UF6 in gaseous phase under atmospheric conditions. Journal of Aerosol Science. 1996;**27**:S405-S406

[20] Shayeganrad G, Mashhadi L. Study of aerosols and molecular extinction effects in ultraviolet DIAL remote sensing in the lower atmosphere. International Journal of Remote Sensing. 2012;**33**:887-904

[21] Csele M. Fundamentals of Light Sources and Lasers. Hoboken, New Jersey: John Wiley & Sons, Inc; 2004

[22] Klett JD. Stable analytical inversion solution for processing lidar returns. Applied Optics. 1981;**20**:211-220

[23] Klett JD. Lidar inversion with variable backscatter/extinction ratios. Applied Optics. 1985; **24**:1638-1643

[24] Rice WW, Oldenborg RC, Wampler FB, Tlee JJ. Gas temperature and density of UF6 determined by two-wavelength UV absorption. Applied Optics. 1981;**20**:2625-2629

[25] Bass AM, Paur aRJ. The ultraviolet cross-section of ozone, results and temperature dependence. In: Atmospheric Ozone, Proceedings of the Quadrennial Ozone Symposium. 1985

[26] Lakowicz JR. Principles of Fluorescence Spectroscopy. 3rd ed. New York: Springer; 2006

[27] Loewen E. Diffraction Grating Handbook. 6th ed: Newport Corporation; 2005